HHS Public Access

Author manuscript

J Control Release. Author manuscript; available in PMC 2018 August 28.

Published in final edited form as:

J Control Release. 2017 August 28; 260: 92–99. doi:10.1016/j.jconrel.2017.05.022.

The Effects of Non-invasive Radiofrequency Electric Field Hyperthermia on Biotransport and Biodistribution of Fluorescent [60]Fullerene Derivative in a Murine Orthotopic Model of Breast Adenocarcinoma

Norman A. Lapin[1,#], **Martyna Krzykawska-Serda**[1,2,#], **Sean Dilliard**[1,3], **Yuri Mackeyev**[4], **Maciej Serda**[4,5], **Lon J. Wilson**[4], **Steven A. Curley**[1,6], and **Stuart J. Corr**[1,4,7,*]

[1]Michael E. DeBakey Department of Surgery, Baylor College of Medicine, Houston, TX 77030, USA [2]Faculty of Biochemistry, Biophysics and Biotechnology, Jagiellonian University, Kraków 30-387, Poland [3]Department of Chemical and Biomolecular Engineering, Rice University, Houston 77005, TX, USA [4]Department of Chemistry, Rice University, Houston 77005, TX, USA [5]Institute of Chemistry, University of Silesia in Katowice, 40-006, Katowice, Poland [6]Department of Mechanical Engineering and Materials Science, Rice University, Houston, TX 77005, USA [7]Department of Biomedical Engineering, University of Houston, Houston 77204, TX, USA

Abstract

The aim of this study is to understand the combined and differential biokinetic effects of radiofrequency (RF) electric-field hyperthermia as an adjunctive therapy to [60]fullerene nanoparticle-based drug delivery systems in targeting the microvasculature and microenvironments of breast cancer tumors. Intravital microscopy (IVM) is an ideal tool to provide the spatial and temporal resolution needed for quantification in this investigation. The water-soluble and fluorescent [60]fullerene derivative (C_{60}-serPF) was designed to be an amphiphilic nanostructure, which is able to cross several biological membranes and accumulate in tumor tissues by passing through abnormally leaky tumor blood vessels. To adequately elucidate the coupled effects of the highly permeable, but heterogeneous tumor vasculature, with the permeabilizing effects of mild (40–42 °C) hyperthermia produced by a local RF field, we controlled variables across tumor and non-tumor mammary gland microvasculature with and without application of RF hyperthermia in each condition. We notice that tumor tissue is characterized by more intense drug extravasation than in contralateral mammary fad pad tissue, which is consistent with enhanced permeability and retention (EPR) effects. The analysis of a

*Corresponding Author: Stuart J. Corr (stuart.corr@bcm.edu).
#joint-first authors

Author Contributions

NL and MKS planed and performed experiments, and wrote the manuscript. MKS, SD, NL and MS analysed the data, MKS performed the statistical evaluation. SJC and SAC conceived the experiment, reviewed the manuscript, and made edits. All authors read and approved the final manuscript.

permeability parameter (P_{app}), C_{60}-serPF velocity, and the time of compound influx into the intra- and extra-vascular space suggest that mild RF hyperthermia can improve nanoparticle delivery into tumor tissue.

Graphical Abstract

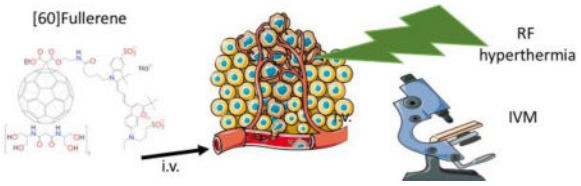

Keywords

[60]Fullerene; hyperthermia; intravital microscopy; drug pharmacokinetics; chemotherapy

Introduction

Drug solubility, lipophilicity, penetration and retention in tumor tissues are longstanding challenges in medicinal chemistry and have been addressed by a variety of methods with varying success[1, 2]. It is essential for pharmacological success of anti-cancer chemotherapy that a sufficient quantity of a drug, injected intravenously, reaches and penetrates tumor tissues, being successfully retained long enough to have cytotoxic effects. Currently, the usage of nanoparticles (NPs) as drug delivery systems (DDS) is an attractive alternative to a standard treatment, due to their several advantages on the molecular level[3]. For example, their high potential for loading a drug into a confined space[4, 5], protection of nanoparticle-bound drugs from degradation[6] and the possibility to engineer specific conjugates for controlled and targeted release into the tumor[2, 7], make them an attractive tool for modern pharmacology. Additionally, NPs conjugated with cytotoxic drugs will modify drug biodistribution and pharmacokinetics leading to optimized drug dosage with decreased cytotoxicity to normal tissues and enhanced activity to cancer[8]. Barriers to delivery and uptake of NPs by tumors include clearance by the mononuclear phagocyte system (MPS)[2, 6], renal clearance[9], high interstitial tumor pressure[1], non-uniform vascular permeability[10] and heterogeneity in intratumoral blood flow[1]. Solutions to these problems have been addressed directly through NP design, by tailoring hydrodynamic size[11] and charge[12] to circumvent these body systems and thereby take advantage of the enhanced penetration and retention (EPR) effect of NPs[2, 13].

Several examples of nanomaterials used as DDS have been combined with hyperthermia treatment to enhance NP delivery to tumors. Kong *et al.* (2000) demonstrated that hyperthermia enables particles of larger size to enter tumor tissues[14]. Hyperthermia treatment has been shown to induce vascular permeability in both tumor and normal tissue[15– 17], potentially facilitating NP extravasation. Hyperthermia has also been employed in combination with chemotherapy[18, 19] and may be applied to the whole body[18] or locally to the target region[20]. Although much work has been spent on investigating nano-mediated hyperthermia techniques based on optical phenomenon such as surface plasmon polariton

resonance[21, 22] these techniques are limited to the treatment of superficial cancers due to the inherently shallow penetration depths across the optical and near infrared spectrum (in the mm range). Radiofrequency electric-field hyperthermia, on the other hand, operating across the radio spectrum (MHz range) affords deep penetration depths on the order of 1 – 30 cm. We have previously shown that RF hyperthermia can also be used alongside antibody-chemotherapy-conjugated gold nanoparticles to enhance the efficacy of the chemotherapy drug, at substantially lower dosages[23, 24], as well as demonstrating the ability for RF energy to remotely trigger drug release from cisplatin-loaded single walled carbon nanotubes[25]. This is in addition to studies demonstrating the ability of RF energy to enhance the uptake of circulating macromolecules into breast tumors based on differential tissue dielectric properties compared to normal, healthy tissue[26, 27]. We anticipate the same effect when used in conjunction with a [60]fullerene-based drug delivery system.

Among available NP choices, [60]fullerene-based drug delivery systems offer ease of drug attachment, due to a good synthetic accessibility *via* cyclopropanation and click reactions[28, 29]. The spherical shape and small size (around 3 nm) make them an interesting scaffold for multi-drug delivery[5, 30]. Interestingly, several reports have shown that shape of nanomaterial has influence on binding modes to mammalian cell membranes, which was profoundly investigated for gold and silica nanoparticles[31]. It was previously reported that [60]fullerene drug conjugates have been studied in terms of fluorescence microscopy, including fluorescence imaging with two-photon excitation, to examine the uptake and distribution in human breast cancer cells[32].

Moreover, our group has synthesized the fullerene conjugate with FDA approved anti-cancer drug Paclitaxel®, which has shown good stability in aqueous solutions (10 % DMSO), being hydrolyzed only after 80 minutes of incubation at 37° C with bovine plasma[30]. Several novel reports describing the [60]fullerenes drug conjugates as convenient drug delivery systems have been published[33– 38], which merits study of their biodistribution through tumor vasculature. The C_{60}-serPF molecule used in this study (Figure 1) was designed to be a highly water-soluble fullerene derivative (having five diserinol malonate units) with significant fluorescent properties in the infrared region, due to chemical conjugation of a fluorescent tag to the [60]fullerene scaffold via formation of an amide bond[39]. The previous studies in our group have shown no cytotoxic effects for synthetic fullerene derivatives especially in cellular and *iv vivo* models, with preferential cell localization of [60]fullerenes in nucleus[39, 40].

Intravital microscopy (IVM) is a powerful tool that can provide detailed real-time information about tumor and drug or NP interactions with high temporal and spatial resolution, critical to understanding the biokinetics of NP delivery and extravasation in tumor microvasculature. IVM employs the optical sectioning power of confocal microscopy to capture real-time delivery of fluorescently-labeled drugs and NPs in the microvasculature of live animals at micron scale resolution in three dimensions. Given the short clearance half-life (on the scale of 15 min) of C_{60}-serPF, as well as its highly variable dynamics in heterogenous tumor tissue[41], the temporal and spatial resolution of IVM (on the scale of a few microns, and 1–2 s or faster) is critical for capturing the behavior of C_{60}-serPF delivery

and extravasation as well as that of other water-soluble fullerenes in the tumor microenvironment.

In this study, we are interested in understanding the effects of controlled mild (40–42°C) radiofrequency hyperthermia (CM-RFH) on the delivery and extravasation kinetics of C_{60}-serPF in the microvasculature of orthotopic breast adenocarcinoma vs. contralateral tissue (non-tumor mammary fat pad) immediately after treatment with CM-RFH. Herein, water-soluble [60]fullerene biokinetics are quantified in terms of vascular permeability within fat pad or tumor tissue via thresholded fluorescence intensity of IVM-extracted metrics. These metrics include apparent permeability ($P_{app;}$ described in Materials and Methods), NP velocity ratio between extra- and intravascular compartments and duration of initial linear velocity of NP vascular efflux prior to kinetic plateau. We hypothesize that applying CM-RFH to tumor vascular in advance of intravenous (i.v.) fullerene NP delivery will result in increased extravasation of [60]fullerenes in the tumor microenvironment.

Materials and Methods

Materials

FITC-Dextran (70kDa) was used as a vasculature tracer; a 10 mg/ml solution in phosphate-buffered saline (PBS) was injected as a single bolus via tail vein catheter. The vascular tracer during IVM imaging was excited by a 488 nm laser and the fluorescence was analysed across the range of 500 to 550 nm. During the imaging session, the standard FITC channel settings were used according to Nikon recommendations.

The C_{60}-serPF was synthesised and purified according to a previously described procedure[30]. The [60]fullerene derivative used in this study is a C_{60}-malonodiserinolamide scaffold conjugated with the red fluorescent dye PromoFluor-633 (C_{60}-serPF), which enabled fluorescence-based tracking and relative quantification of highly water soluble C_{60}-ser. In all experiments C_{60}-serPF was injected i.v. at 4 mg/kg body weight as a single bolus. In order to analyse C_{60}-serPF biokinetics during IVM imaging the standard settings for Cy5 channel were used according to the manufacturer, with excitation at 640 nm and fluorescence emission from 662 to 738 nm.

Ethics statement

All experiments were performed with the approval of the Institutional Animal Care and Use Committee (IACUC) at Baylor College of Medicine and established protocols followed.

Tumour model

Female Balb/c athymic FoxN1 nude mice were housed under standard conditions with free access to food and water. When animals were 8–12 weeks old, 10^5 4T1 cells suspended in 50 μl of serum free medium were injected into the left inguinal mammary fat pad. The 4T1 cells were maintained, prepared and injected according to the Pulaski and Ostrand-Rosenberg protocol[42]. The rationale of choosing nude mice for the experiments is to avoid shaving before the imaging which can affect skin and/or surrounding tissue vasculature.

Animal preparation

The animal preparation was described and presented in detail in our recent study[41]. During all procedures animals were kept in a deep (surgery level) plane of anaesthesia with 1–4% isoflurane. The first step required placement of a tail vain catheter (24G i.v. catheter with inserted stretched PE10 Intramedic polyethylene tubing). The catheter was secured by tape and kept functional throughout the experiment by injection of 1% heparin solution in saline. Next, skin-flap surgery was performed and tumour surface with visible vasculature was exposed. Care was taken to maintain hydration of exposed areas using PBS. After that, the animal was placed on an imaging table kept warm via heat lamp (41 °C surface temperature). The IVM system was grounded with the copper tape, and the representative field of view was chosen (containing tumour or normal vasculature in tumour or fat pad tissue). To evaluate C_{60}-serPF extravasation we studied mice with 4T1 tumours treated by RF (N=3) compared to mice treated without RF irradiation (N=6). Contralateral mammary fat pad was chosen as control tissue (EPR effect no present) under three conditions: 1 and 2) with (N=2) and without (N=2) RF exposure in tumour-bearing mice and 3) without RF exposure in a mouse without cancer (N=2).

IVM imaging platform with portable RF device

The mouse imaging and RF treatment station was localised under the IVM lens (16X) and between the transmission (TX) and reception (RX) antennas of the RF system, allowing imaging during CM-RFH treatment. The RF-IVM hyperthermia-imaging platform is described in significant detail in our previous work[27, 41]. During imaging mouse core temperature was monitored via rectal probe. The tumour, mammary fat pad and surrounding tissue temperatures were monitored continuously by infra-red (IR) camera (FLIR SC 6000, FLIR Systems, Inc., Boston, MA). The FITC-Dextran solution was injected i.v. (10 mg/kg BW) followed by CM-RFH treatment and subsequently, administration of C_{60}-serPF. All injections were performed at 10 μl/s during active IVM image data acquisition so all influx kinetics could be analysed together. The IVM laser power and gain were optimised for each imaging session because of varying shape and optical tissue properties. Therefore, the recorded fluorescence intensity was normalised to the maximum of the fluorescence signal in all data. Additionally, this technique makes direct comparison of accumulated compounds in the selected field of view manageable.

RF hyperthermia

A portable RF device was used to generate tumour or mammary fat pad hyperthermia in a non-invasive way. The device has a fixed-frequency (13.56 MHz) and is powered up to 200 W by a water-cooled power supply (Seren, RX01/LX01 Series, Industrial Power Systems, Inc.) connected via a high-current carrying capacity 50 Ω co-axial cable. The treatment was initiated at 10 W operating power and gradually increased to 50–75 W over 5 min. When tumour surface temperature (measured by IR camera, FLIR SC 6000, FLIR Systems, Inc., Boston, MA) was 41°C the RF power was continuously adjusted to maintain this temperature for 10 min. After RF irradiation was complete, IVM imaging was continued for 10 – 30 min or longer.

Image and data analysis

Analysis of the IVM images was performed using Nikon NIS Elements software. A replicable, binary thresholding technique was developed to partition the images into intravascular and extravascular regions. The vascular region was determined by binary thresholding of the FITC channel. Selection of threshold intensity levels was determined by evaluation of "least frequent" image histogram intensity values yielding the most reasonable threshold region. Typically, five binary threshold values were sampled to identify optimal region features. Based on qualitative observations, pixels fluorescing at these values tended not to be noise or auto-fluorescence. A 1x smooth and 1x clean operation was employed to filter out noise to finish creating the vascular mask; then the area of the vascular mask was measured. The procedure was repeated for each of the threshold values corresponding to varying percentages of least frequent intensity values, and the change in mask area with respect to least frequent percentage was computed. The percentage value corresponding to the local minimum of this rate of change was selected to define the binary threshold for the vascular mask because it represents a well-defined area that does not readily change by increasing the size of the threshold.

Apparent permeability, P_{app}, is a transport parameter frequently used to characterize the diffusion of a chemical species across a membrane. A higher value of P_{app} corresponds to a higher tendency of a specific species to diffuse across a particular membrane. Thus, this parameter was used to characterize the efflux of NPs from the intra- to extravascular region in the IVM images. It was assumed that diffusion was the primary mechanism of transport. As we cannot differentiate between transport mechanisms of extravasation using IVM, apparent permeability also lumps in the small effects of advection on NP transport. The apparent permeability can be derived by using a modified form of Fick's first law of diffusion (Equation 1):

$$J_{ex} = P_{app} A_v \Delta c_{ie} \quad \text{Equation 1}$$

where J_{ex} is the efflux of C_{60}-serPF, $\boldsymbol{A_v}$ is the perimeter wall area between intra- and extravascular regions in the field of view (FOV) of the image sequence and $\boldsymbol{\Delta c_{ie}}$ is the concentration gradient across intra- to extravascular compartments.

Rearrangement of the above expression allows P_{app}, to be calculated from experimental data of the mass flux of NPs into the extravascular region and the concentration gradient of NPs between the intra- and extravascular regions. Due to the proportionality of fluorescent intensity and concentration by the Beer-Lambert Law, the following expression (Equation 2) was used to calculate apparent permeability from IVM image data:

$$P_{app} = \frac{V_{ex} \frac{dI_{ex}}{dt}}{A_v (I_{in} - I_{ex})} \quad \text{Equation 2}$$

where V_{ex} is the volume of the extravascular region in the image sequence FOV, $\frac{dI_{ex}}{dt}$ is the instantaneous rate of change of C_{60}-serPF fluorescent intensity in the extravascular region and $\boldsymbol{I_{in} - I_{ex}}$ is the instantaneous C_{60}-serPF intensity difference between intra- and extra-vascular regions in the FOV.

The apparent permeability was computed based on global rather than local image data (across the entire FOV rather than at specific regions) using a protocol, which follows the method for determining a vascular mask. However, this expression was only valid when the NP was localised to the vasculature and the area immediately outside of it; this occurred during the first few instants of extravasation. The average apparent permeability was calculated for the initial image frames where extravasation was first observed in the IVM images for the five binary threshold values that were sampled. These five apparent permeability values were computed to finally characterize the permeability of the vasculature within the FOV for a particular animal. This expression assumes that the volume of the extravascular region and the interfacial surface area of the blood vessels are constant with respect to time. Furthermore, this expression assumes that the concentration gradient and permeability are invariant in space; as a result, it was deemed to be an effective parameter for describing global but not local behaviours.

Statistical analysis

For statistical data processing, Statistica12® was used and the U-test and factorial ANOVA were performed. Used three way effects ANOVA allow to analyse the high-order interactive effects of multiple categorical independent variables. The Kurskal-Wallis nonparametric test was used to determine the statistical significance between particular experimental groups.

Results

To understand the extravasation of C_{60}-serPF into the breast tumor microenvironment under RF hyperthermia two types of vasculature were compared: (1) 4T1 breast tumor vasculature (mainly at the superficial part of the tumor), and (2) non-tumor vasculature present in the mammary fat pad of either tumor-bearing or normal mice. The 4^{th} inguinal mammary fat pad was selected as the orthotopic location for both 4T1 tumor and control fat pad tissues, based on ease of tumor access and clear tumor-fat pad-skin boundaries. In our study, we found that C_{60}-serPF generally extravagates more in tumor vasculature and application of RF can enhance this effect (Figures 2, 4, 5). On the other hand, extravasation of the compound in tumor tissue is very heterogeneous with areas of both poor and extremely high leakage into the extravascular space. Additionally, tumor vascular dimensions shown are highly variable and exhibit differential progression of C_{60}-serPF leakage compared to fat pad vasculature. These observations are crucial for designing the novel DDS based on a [60]fullerene scaffold, since anti-cancer drugs, which will be conjugated with fullerene via cleavable spacers could be more efficiently delivered into tumor tissues. Moreover, elevation of the temperature caused by RF treatment could increase the cleavage of ester or amide linkage and enhance targeted delivery of biologically active cargo.

Figure 2 shows representative images of fat pad and tumor microenvironments differentially pre-treated with CM-RFH before and after delivery of C_{60}-serPF at both early (linear region) and late (plateau region) post injection time points. Upon quantification of intravascular (Fig. 2 - green) and extravascular (Fig. 2 - white) compartments defined by presence or absence of FITC-Dextran vascular tracer, relative fluorescence of C_{60}-serPF through those regions was tracked over time. Limitations on the utility of the 70 kDa FITC-Dextran as a vascular tracer depend on the timescale of observation, the condition of the vasculature and the fluorescence and absorption spectra of the conjugated FITC dye. Normal vasculature exhibits a very low diffusion rate of albumin (similar in size to this tracer) compared to that of water, while tumor vasculature has substantially more permeability to macromolecules in this size range [NAGY]. However, due to the far smaller size of C_{60}-serPF with rapid extravasation on the scale of seconds, any leakage of FTIC-Dextran on the same timescale is negligible, where significant loss of ~70 kDa particles occurs on the scale of longer than five minutes[10, 43, 44]. It is worth mentioning though that during the experiments (data not shown) we discovered that exposure to temperatures equal or higher than 42°C leads to significant leakage of FITC-Dextran from the intravascular space (occurring when vessel size appeared to grow rapidly and vessel shape and contours dispersed within a matter of seconds). In terms of the use of fluorescence to quantify relative concentrations of C_{60}-serPF in intra- versus extravascular compartments, the spectral bands of C_{60}-serPF and FTIC-Dextran exhibit excellent separation.

Given the variability in vascular dimensions across FOVs analyzed in this study, it is worth briefly considering the effects that vascular geometric dimensions, pressure gradients and biological mechanisms can have on NP and fluid transport and permeability within tumor versus non-tumor microvasculature and surrounding tissues. Certain features of vascular geometry, such as fractal dimension and vascular density, have been shown to correlate positively with increased extravasation of NPs in intratumoral microenvironments while exhibiting a high degree of heterogeneity within and between tumors as evidenced by high variance of measurements[43]. Chronic hyperpermeability of tumor vasculature also occurs due to permeabilization of vessels by vascular endothelial growth factor, released in tumor angiogenesis[10]. Such stimulation results in formation of mother vessels with diameters up to 4–5 times that of normal vessels, having greatly thinned vascular endothelium and fenestrae, openings with diameters ranging from 70–150 nm[10].

As a means of neutralizing these complex and interrelated effects with high variability and heterogeneity, this study employs the metric, P_{app} in a two-compartment model (intravascular and extravascular space) to monitor transport across tumor microvasculature. Since the parameters contributing to P_{app}, namely compartment volume, total area of the perimeter wall between compartments and summed intensity of NP fluorescence are measured for the entire FOV, P_{app} is independent of vascular dimensions, and therefore a robust metric for evaluation of overall vascular permeability within the tumor microenvironment.

Fig. 3 shows representative images of the change in summed C_{60}-serPF fluorescence intensity with time within intra- and extravascular compartments for tumor and fat pad with and without CM-RFH treatment. During image processing, after intra- and extravascular

regions were defined, appropriate fluorescence thresholds were applied to quantify the kinetics of the C_{60}-serPF. To compare the biotransport kinetics between animals, normalization to the highest observed fluorescence signal was performed (as presented in Fig. 3). We confirm that application of non-invasive CM-RFH enhanced the extravasation of C_{60}-serPF especially in the tumor vasculature. Non-tumor vasculature also responded to CM-RFH with enhanced permeability of C_{60}-serPF. As presented in Fig. 3, the extravascular C_{60}-serPF relative fluorescence kinetics were highest in tumor tissue after CM-RFH application. In the case shown the effect of RF hyperthermia is highly significant and affects the time-to-maximum of C_{60}-serPF fluorescence intensity in the extravascular space and total compound accumulation. To evaluate compound extravasation, three parameters were calculated: (1) apparent permeability – P_{app} to calculate NP efflux (Fig. 4, (2) ratio of extra-/intravascular velocity of C_{60}-serPF during influx into the tissue (Fig. 5) and (3) ratio of time needed to reach the plateau of C_{60}-serPF fluorescence intensity in extra- versus intravascular region within the tissue (Fig. 6).

The apparent permeability, P_{app}, analyzed based on the initial rates of extravasation, is a quantification of the diffusion coefficient of NP crossing the boundary between intra- and extravascular regions. Fig. 4 compares P_{app} between tumor and non-tumor tissues with and without RF treatment. The increase of mean values of P_{app} was observed in both tumor ($p=0.0153$) and fat pad tissues ($p=0.0003$) as a result of CM-RFH treatment. In the absence of CM-RFH treatment, P_{app} was significantly higher in tumor than fat pad ($p=0.021$). The comparison of RF hyperthermic effects on contralateral mammary fat pads between mice with and without tumors indicates that potential metastasis to the contralateral fat pad had no effect on the apparent permeability of C_{60}-serPF.

The linear regions of the graphs of normalized C_{60}-serPF fluorescence intensity in the intra- and extravascular space (Fig.3) were analyzed independently for each curve, followed by calculation of C_{60}-serPF influx velocity and total time of influx to the intra- and extravascular regions. Next, the ratio of C_{60}-serPF velocities in extra- to intravascular regions, and total linear influx times were calculated and analyzed by experimental group as presented in Figs. 5 and 6. After CM-RFH treatment, increases in P_{app} and velocity ratio for both tumor and fat pad tissues were observed. It is worth noting that the mean ratio of C_{60}-serPF extra-/intravascular velocities is highest for tumor tissue treated with RF hyperthermia. The observed extra-/intravascular C_{60}-serPF velocity ratios in Fig. 5 are <1, indicating that greater mass of C_{60}-serPF is delivered to the intravascular space than mass that moves from the intra- to extravascular space. However, in CM-RFH treated tumor tissue, this ratio is closer to 1, suggesting that more NP is transferred from the intra- to the extravascular space compared with other groups. The higher the ratio, the higher the velocity of C_{60}-serPF into the extravascular space.

Duration of linear region of C_{60}-serPF influx into the extravascular space presented as a ratio (Fig. 6) was lower after CM-RFH treatment in both tissue types suggesting much faster C_{60}-serPF penetration into extravascular space from the intravascular region. The higher the ratio, the more time is needed for C_{60}-serPF to obtain the maximum possible concentration in the extravascular space.

Discussion

In this study, the effect of applying CM-RFH treatment to tumor tissue versus non-tumor orthotopic mammary fat pad tissue on [60]fullerene NP delivery and accumulation kinetics was assessed. While significance levels were largely not reached in individual comparisons between groups (statistics calculated based on average mouse value) for influx analysis (Figs. 5 and 6), it is reasonable to claim relevance of the RF effects on enhancing NP extravasation due to significant difference of Papp. It is worth mentioning, that the experimental results may be at least partially masked by a high degree of variability in many factors, especially tumor blood vessel dimensions, variability in RF penetration depth and dose applied to imaged tissue regions, and variability in imaging parameters that could dynamically effect fluorescence intensity and positional fidelity. Nonetheless, we observed that the mean value of every parameter tested moved in the direction of increased permeability with CM-RFH treatment prior to C_{60}-serPF injection, suggesting that CM-RFH exhibited a real effect on vascular permeability to this NP.

Mean values of metrics including apparent permeability, efflux velocity, and duration of linear kinetics tended toward behavior indicative of vascular damage due to CM-RFH, leading to faster and increased permeability. Vascular damage has been observed previously in RF-induced hyperthermia, with microvascular injury and increased vascular permeability in both tumor and normal tissue[16] as well as narrowing of endothelial cells[17], possibly suggesting a means of increasing space between cells. Another study showed that hyperthermia could increase permeability of liver tumor vasculature more than normal liver tissue[15]. Such increases in vascular permeability suggest that CM-RFH treatment could potentially enhance intratumoral penetration of drug-loaded NPs. Indeed, the 70 kDa vascular tracer also extravasated in some cases during RF hyperthermia[41] which may suggest underestimation of C_{60}-serPF leakage.

Rapid penetration and retention of drug delivery systems is critical for therapeutic effects in which both components reach tumor cells and remain long enough to exhibit sufficient toxic effects. It has previously been reported that C_{60}-serPF renal clearance times occur on the scale of 15 min[39]. The macrophage phagocytic system (MPS) can rapidly remove NPs from circulation, and renal clearance of particles of C_{60}-serPF size (3 nm hydrodynamic diameter) can be as high as 9 minutes[9]. Therefore, increased vascular permeability by non-invasive CM-RFH has the potential to provide a critical increase in the speed of NP tumoral uptake via extravasation. Furthermore, given the heterogeneity of tumor vasculature permeability, increases in tumor vascular damage, porosity and/or overall permeability might possibly help to normalize region-to-region variability in these measures of tumor blood vessel leakiness to NPs. It is also noteworthy that IVM investigation of C_{60}-serPF extravasation is extremely valuable due to the very fast pharmacokinetic profile of this NP (~3 min after NP injection, strong fluorescence intensity is observed in mouse urine, data not shown).

The nanoparticle size range at which the EPR effect takes place has been cited at approximately 10–100 nm in diameter[45] with maximal uptake from 40–70 kDa[44]. As a single molecule, C_{60}-ser and fluorescent dye conjugated C_{60}-serPF are ~2.2 and ~2.8 kDa, measuring ~3 nm in diameter. The C_{60}-ser molecule has been observed to form

aggregates [39, 46] observed by Differential Light Scattering (DLS) in water, which exist in a wide range of sizes, with estimates of a majority of aggregates from 100–400 nm in diameter[46]. Given the size range of C_{60}-ser aggregates with a sizeable proportion above 100 nm dia., and the possibility that these may exist *in vivo* intravenously, RF enhancement of vascular permeability may increase the EPR effect for C_{60}-ser aggregates within and above the normal range of particle sizes for EPR. Our data suggests that such an effect does occur with significance between CM-RFH and non-CM-RFH treated groups.

The main limitation of reliance on the EPR effect for NP delivery is heterogeneity of tumor vascular permeability both within and between tumors, where some regions may lack any permeability at all [1, 10], leading to non-uniform drug delivery. The dynamic variability and unpredictability of C_{60}-ser aggregation further contribute to limitations on the effective use of EPR. Other factors that affect permeability such as charge (or zeta potential), also known to vary with C_{60}-ser aggregation state[46] and may also contribute to EPR usage limitations. A limitation of CM-RFH treatment of tumor vasculature is that normal vasculature exposed to the treatment also experiences some increase in permeability (Fig. 4). This effect potentially counteracts the advantage of specificity given by EPR, although it would be limited to the region near the tumor and thus not likely be a problem systemically.

Limitations of IVM include invasiveness of the procedure (skin-flap surgery) and ability to analyze only superficial vasculature (imaging depth ~50–100 μm[41]. We suspect that some of the superficial vessels may be affected during tissue layer separation; therfore special care was taken to image only well preserved vessels.

The selected tumor model, breast adenocarcinoma, is a perfect candidate for this analysis due to ease of skin-flap preparation and good access to both orthotopic breast cancer and normal contralateral mammary fat pad tissue.

We discovered IVM predominance as a technique for quantification of C_{60}-serPF biodistribution and pharmacokinetics versus different techniques such as IVIS, homogenate fluorescence or IHC for a number of reasons. IVM is the only technique that provides micron-scale spatial localization of both the vasculature and extravascular space *in vivo* based on both high imaging resolution and spatial selection of the optical slice, a key feature of confocal imaging. IVM further provides a high-resolution snapshot of tumor microenvironment nanoparticle distribution in the first seconds to minutes of extravasation and longer.

By comparison, there are a number of limitations to *ex vivo* analysis of nanoparticle kinetics and biodistribution. First, since extravasation dynamics occur on the scale of seconds, it would be very difficult to freeze or perfuse tissue with fixative to capture various states at the time resolution at which the changes are taking place. Secondly, in reference to immunohistochemistry, since nanoparticles are free to move through tissues, there may be some degree of dispersion from their original biodistribution within tumor tissue that may occur during preservation methods.

Tissue homogenization can provide quantification of nanoparticle uptake into the entire tumor at various time points. An important aspect to consider is that true tumor uptake

should only include extravasated NP and thereby exclude any nanoparticle present in the tumor blood volume. This can potentially be achieved by delaying tumor extraction until later time points when NP extravasation is more complete and blood volume has largely undergone renal clearance, such as e.g. at 60 min post-injection. However, such accommodations may be problematic for direct comparison to IVM, since such timescales are an order o f magnitude greater than those of IVM. Furthermore, when we did attempt homogenization and solvent extraction of the post-injected tissue, we found that the signal of the C_{60}-serPF fluorescence spectrum was too weak to be detected above noise on a spectrophotometer.

In the future, the IVM experiments could be repeated with endothelial cells immunolabeled in advance. While this may add some detail to the process of extravasation and crossing of the vascular barrier, additional information about the dynamics may be limited since the intra/extravascular border is already quite well defined by the tracer, which experiences negligible within the timescale of the video.

For additional spatial information IVIS has even further limits on nanoparticle localization. First, it can only provide a macroscopic view of tumor and systemic uptake and distribution and second it is limited in its ability to provide spatial localization, giving only a two-dimensional overlay. Systemic distribution of C_{60}-serPF by IVIS has been previously provided in Raoof et al., 2013. IVIS also faces the same issue with inability to exclude blood volume as well. Given the low signal intensity of C_{60}-ser-PF in macroscopic amounts of tissue, ability to detect C_{60}-serPF with this method through more layers of tissue of an animal seems unlikely.

Conclusions

Cancer heterogeneity and abnormal tumor vasculature result in non-optimal biodistribution and pharmacokinetics of clinically available cancer drugs leading to problems with drug resistance, inefficient drug localization inside the tissue, and exacerbation of side-effects. One possible solution is the use of nanoparticles as drug delivery systems for anti-cancer drugs. In our study we demonstrated that C_{60}-serPF could be used as a model delivery system for biodistribution studies of [60]fullerene anti-cancer conjugates due to its preferred biokinetic profile. The analysis of independent parameters such as P_{app} and C_{60}-serPF influx velocity and time indicate that C_{60}-serPF extravasates more into orthotopic breast tumor tissue than into contralateral mammary fad pad. Additionally, we showed that non-invasive RF induced, mild hyperthermia can significantly enhance C_{60}-serPF extravasation. It is noteworthy that pathological tumor vasculature responds to RF hyperthermia treatment which has the potential to enhance drug biodistribution inside tumor tissue.

Acknowledgments

NL, MKS, SD, MS, SAC, and SJC acknowledge the funding of Kanzius Foundation and NIH U54CA143837. SD thanks the Baylor Summer Medical and Research Training Program for providing funding and the opportunity to work at Baylor College of Medicine. LJW also thanks the Welch Foundation (Grant C-0627) for support.

ABBREVIATIONS

IVM	intravital microscopy
C_{60}-serPF	[60]fullerene serinol malonate pentakis-adduct – PromoFluor-633 conjugate
i.v.	intravascular
BM	body mass
NPs	nanoparticles
t	time
IVIS	IVIS®. Spectrum in vivo imaging system
IHC	immunohistochemistry
RF	radiofrequency
P_{aap}	apparent permeability
DDS	drug delivery system
CM-RFH	controlled mild hyperthermia generated by radiofrequency field
IR	infrared
TX	transmission antenna of RF system
RX	reception antenna of RF system

References

1. Jain R. Delivery of Molecular and Cellular Medicine to Solid Tumors. Adv. Drug Deliv. Rev. 2012:997–1003.
2. Nie S. Understanding and Overcoming Major Barriers in Cancer Nanomedicine. Nanomedicine (Lond). 2010; 5:523–528. [PubMed: 20528447]
3. Faraji AH, Wipf P. Nanoparticles in Cellular Drug Delivery. Bioorg. Med. Chem. 2009; 17:2950–2962. [PubMed: 19299149]
4. Chu KS, Schorzman AN, Finniss MC, Bowerman CJ, Peng L, Luft JC, Madden AJ, Wang AZ, Zamboni WC, DeSimone JM. Nanoparticle Drug Loading as a Design Parameter to Improve Docetaxel Pharmacokinetics and Efficacy. Biomaterials. 2013; 34:8424–8429. [PubMed: 23899444]
5. Mackeyev Y, Raoof M, Cisneros B, Koshkina NSBC, Wilson LJ, Curley SA. Toward Paclitaxel-[60]Fullerene Immunoconjugates as a Targeted Prodrug against Cancer. Nanosyst. Physics, Chem. Math. 2014; 5:67–75.
6. Singh1 R, Lillard JJW. Nanoparticle-Based Targeted Drug Delivery. 2012; 86:215–223.
7. Singh RWLJ. Nanoparticle-Based Targeted Drug Delivery. Exp. Mol. Pathol. 2009; 86:215–223. [PubMed: 19186176]
8. Hubbell JA, Chilkoti A. Nanomaterials for Drug Delivery. Science (80-.). 2012; 337:303–305.
9. Michelle Longmire, Peter L., Choyke, MD., Hisataka Kobayashi, MDP. Clearance Properties of Nano-Sized Particles and Molecules as Imagin Agents: Consideration and Caveats. 2012; 3:703–717.
10. Nagy JA, Benjamin ÆL, Zeng ÆH, Dvorak AM, Dvorak ÆHF. Vascular Permeability. Vascular Hyperpermeability and Angiogenesis. 2008:109–119. [PubMed: 18293091]

11. Yuan F, Dellian M, Fukumura D, Leunig M, Berk Da, Torchilin VP, Jain RK. Vascular Permeability in a Human Tumor Xenograft: Molecular Size Dependence and Cutoff Size Advances in Brief Vascular Permeability in a Human Tumor Xenograft: Molecular Size Dependence and Cutoff Size1. Cancer Res. 1995; 55:3752–3756. [PubMed: 7641188]
12. Dellian M, Yuan F, Trubetskoy VS, Torchilin VP, Jain RK. Vascular Permeability in a Human Tumour Xenograft: Molecular Charge Dependence. Br. J. Cancer. 2000; 82:1513–1518. [PubMed: 10789717]
13. Fang J, Nakamura H, Maeda H. The EPR Effect: Unique Features of Tumor Blood Vessels for Drug Delivery, Factors Involved, and Limitations and Augmentation of the Effect. Adv. Drug Deliv. Rev. 2011; 63:136–151. [PubMed: 20441782]
14. Kong G, Braun RD, Dewhirst MW. Hyperthermia Enables Tumor-Specific Nanoparticle Delivery: Effect of Particle Size Hyperthermia Enables Tumor-Specific Nanoparticle Delivery: Effect of Particle Size 1. Cancer Res. 2000; 60:4440–4445. [PubMed: 10969790]
15. Gnant MFX, Noll LA, Terrill RE, Wu PC, Berger AC, Nguyen HQ, Lans TE, Flynn BM, Libutti SK, Bartlett DL. Isolated Hepatic Perfusion for Lapine Liver Metastases Impact of Hyperthermia on Permeability of Tumor Neovasculature. :890–899.
16. Nikfarjam M, Muralidharan V, Malcontenti-wilson C. Progressive Microvascular Injury in Liver and Colorectal Liver Metastases Following Laser Induced Focal Hyperthermia Therapy. 2005; 73:64–73.
17. Kawai N, Kobayashi D, Yasui T, Umemoto Y, Mizuno K, Okada A, Tozawa K, Kobayashi T, Kohri K. Evaluation of Side Effects of Radiofrequency Capacitive Hyperthermia with Magnetite on the Blood Vessel Walls of Tumor Metastatic Lesion Surrounding the Abdominal Large Vessels An Agar Phantom Study. 2014:1–8.
18. Wust P, Hildebrandt B, Sreenivasa G, Rau B, Gellermann J, Riess H, Felix R, Schlag P. Hyperthermia in Combined Treatment of Cancer. Lancet Oncol. 2002; 3:487–497. [PubMed: 12147435]
19. van der Zee J. Heating the Patient: A Promising Approach? Ann. Oncol. 2002; 13:1173–1184. [PubMed: 12181239]
20. Cheung AY, Neyzari A. Deep Local Hyperthermia for Cancer Therapy. External Electromagnetic and Ultrasound Techniques1. 1984:44.
21. Liu C, Mi CC, Li BQ. The Plasmon Resonance of a Multilayered Gold Nanoshell and Its Potential Bioapplications. IEEE Trans. Nanotechnol. 2011; 10:797–805.
22. Zheng YB, Kiraly B, Weiss PS, Huang TJ. Molecular Plasmonics for Biology and Nanomedicine. Nanomedicine. 2012; 7:751–770. [PubMed: 22630155]
23. Raoof M, Corr SJ, Kaluarachchi WD, Massey KL, Briggs K, Zhu C, Cheney MA, Wilson LJ, Curley SA. Stability of Antibody-Conjugated Gold Nanoparticles in the Endolysosomal Nanoenvironment: Implications for Noninvasive Radiofrequency-Based Cancer Therapy. Nanomedicine Nanotechnology, Biol. Med. 2012; 8:1096–1105.
24. Raoof M, Corr SJ, Zhu C, Cisneros BT, Kaluarachchi WD, Phounsavath S, Wilson LJ, Curley SA. Gold Nanoparticles and Radiofrequency in Experimental Models for Hepatocellular Carcinoma. Nanomedicine Nanotechnology, Biol. Med. 2014; 10:1121–1130.
25. Raoof M, Cisneros BT, Guven A, Phounsavath S, Corr SJ, Wilson LJ, Curley SA. Remotely Triggered Cisplatin Release from Carbon Nanocapsules by Radiofrequency Fields. Biomaterials. 2013; 34:1862–1869. [PubMed: 23228421]
26. Raoof M, Cisneros BT, Corr SJ, Palalon F, Curley SA, Koshkina NV. Tumor Selective Hyperthermia Induced by Short-Wave Capacitively-Coupled RF Electric-Fields. PLoS One. 2013; 8:e68506. [PubMed: 23861912]
27. Corr SJ, Shamsudeen S, Vergara LA, Ho JC-S, Ware MJ, Keshishian V, Yokoi K, Savage DJ, Meraz IM, Kaluarachchi W, et al. A New Imaging Platform for Visualizing Biological Effects of Non-Invasive Radiofrequency Electric-Field Cancer Hyperthermia. PLoS One. 2015; 10:e0136382. [PubMed: 26308617]
28. Maggini M, Scorrano G, Prato M. Addition of Azomethine Ylides to C60: Synthesis, Characterization, and Functionalization of Fullerene Pyrrolidines. J. Am. Chem. Soc. 1993; 115:9798–9799.

29. Iehl J, de Freitas RP, Nierengarten J-F. Click Chemistry with Fullerene Derivatives. Tetrahedron Lett. 2008; 49:4063–4066.
30. Zakharian TY, Seryshev A, Sitharaman B, Gilbert BE, Knight V, Wilson LJ. A Fullerene - Paclitaxel Chemotherapeutic: Synthesis, Characterization, and Study of Biological Activity in Tissue Culture. J. Am. Chem. Soc. 2005; 127:12508–12509. [PubMed: 16144396]
31. Chithrani BD, Ghazani AA, Chan WCW. Determining the Size and Shape Dependence of Gold Nanoparticle Uptake into Mammalian Cells. Nano Lett. 2006; 6:662–668. [PubMed: 16608261]
32. Liu J-H, Cao L, Luo PG, Yang S-T, Lu F, Wang H, Meziani MJ, Haque SA, Liu Y, Lacher S, et al. Fullerene-Conjugated Doxorubicin in Cells. ACS Appl. Mater. Interfaces. 2010; 2:1384–1389. [PubMed: 20420365]
33. Partha R, Mitchell LR, Lyon JL, Joshi PP, Conyers JL. Buckysomes: Fullerene-Based Nanocarriers for Hydrophobic Molecule Delivery. ACS Nano. 2008; 2:1950–1958. [PubMed: 19206436]
34. Bhirde AA, Patel V, Gavard J, Zhang G, Sousa AA, Masedunskas A, Leapman RD, Weigert R, Gutkind JS, Rusling JF. Targeted K illing of Cancer Cells in Vivo and in Vitro with EGF-Directed Carbon Nanotube-Based Drug Delivery. ACS Nano. 2009; 3:307–316. [PubMed: 19236065]
35. Montellano A, Da Ros T, Bianco A, Prato M. Fullerene C60 as a Multifunctional System for Drug and Gene Delivery. Nanoscale. 2011; 3:4035. [PubMed: 21897967]
36. Shi J, Yu X, Wang L, Liu Y, Gao J, Zhang J, Ma R, Liu R, Zhang Z. PEGylated Fullerene/iron Oxide Nanocomposites for Photodynamic Therapy, Targeted Drug Delivery and MR Imaging. Biomaterials. 2013; 34:9666–9677. [PubMed: 24034498]
37. Shi J, Zhang H, Wang L, Li L, Wang H, Wang Z, Li Z, Chen C, Hou L, Zhang C, et al. PEI-Derivatized Fullerene Drug Delivery Using Folate as a Homing Device Targeting to Tumor. Biomaterials. 2013; 34:251–261. [PubMed: 23069706]
38. Shi J, Wang B, Wang L, Lu T, Fu Y, Zhang H, Zhang Z. Fullerene (C60)-Based Tumor-Targeting Nanoparticles with “off-On” State for Enhanced Treatment of Cancer. J. Control. Release. 2016; 235:245–258. [PubMed: 27276066]
39. Raoof M, Mackevey Y, Cheney MA, Wilson LJ, Curley SA. Internalization of C60 Fullerenes into Cancer Cells with Accumulation in the Nucleus via the Nuclear Pore Complex. Biomaterials. 2012; 33(10):2952–2960. [PubMed: 22245558]
40. Sayes, Christie M., Fortner, John D., Guo, Wenh, Lyon, Delina, Boyd, Adina M., Ausman, Kevin D., Tao, Yizhi J., Sitharaman, Balaji, Wilson, Lon J., Hughes, Joseph B., West, Jennifer L., Colvin, VL. The Differential Cytotoxicity of Water-Soluble Fullerenes. Nano Lett. 2004; 4:1881–1887.
41. Lapin NA, Krzykawska-Serda M, Ware MJ, Curley SA, Corr SJ. Intravital Microscopy for Evaluating Tumor Perfusion of Nanoparticles Exposed to Non-Invasive Radiofrequency Electric Fields. Cancer Nanotechnol. 2016; 7:5. [PubMed: 27429662]
42. Pulaski, BA., Ostrand-Rosenberg, S. Current Protocols in Immunology. John Wiley & Sons, Inc.; Hoboken, NJ, USA: 2001. Mouse 4T1 Breast Tumor Model; p. 1-16.
43. Reitan NK, Thuen M, Goa PE, de Lange Davies C. Characterization of Tumor Microvascular Structure and Permeability: Comparison between Magnetic Resonance Imaging and Intravital Confocal Imaging. J Biomed Opt. 2010; 15:36004.
44. Dreher MR, Liu W, Michelich CR, Dewhirst MW, Yuan F, Chilkoti A. Tumor Vascular Permeability, Accumulation, and Penetration of Macromolecular Drug Carriers. J. Natl. Cancer Inst. 2006; 98:335–344. [PubMed: 16507830]
45. Petros RA, DeSimone JM. Strategies in the Design of Nanoparticles for Therapeutic Applications. Nat. Rev. Drug Discov. 2010; 9:615–627. [PubMed: 20616808]
46. Cheney, MA. Radiofrequency-Induced Cellular Hyperthermia: Water- Soluble Fullerene as a New Cancer Therapeutic Agent (Unpublished Doctoral Dissertation). Rice University; Houston: 2014. Retrieved from https://scholarship.rice.edu/handle/1911/77171

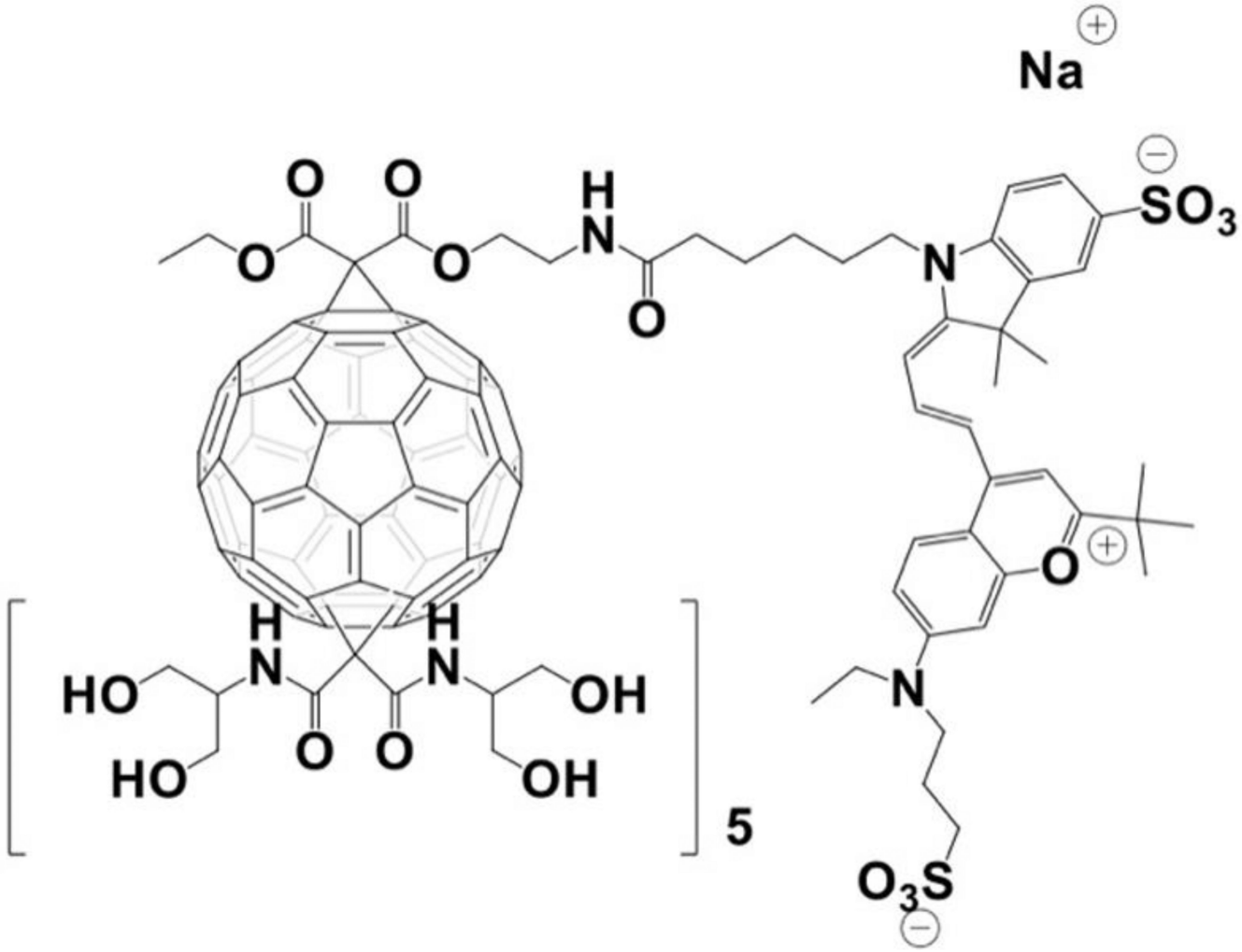

Figure 1.
The chemical structure of C_{60}serPF.

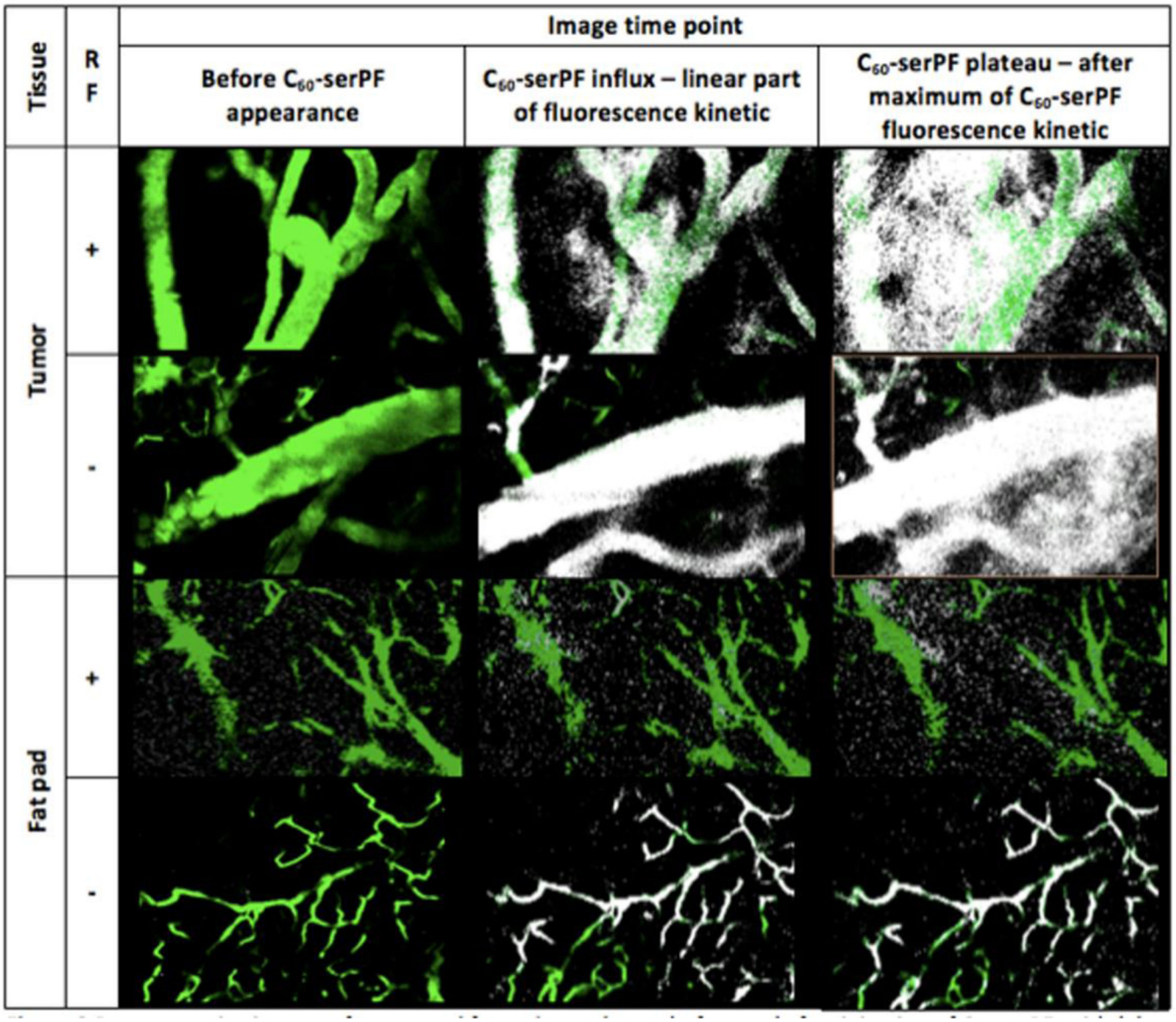

Figure 2.

Representative images of tumor and fat pad vasculature before and after injection of C_{60}-serPF, with (+) or without (−) RF treatment. FITC-Dextran (70 kDa) was used as a vascular tracer (green) and C_{60}-serPF fluorescence is presented in white. The selected frames represent three time points: (1) before C_{60}-serPF appeared in the FOV, (2) during influx of C_{60}-serPF into blood vessels in the FOV (the linear region of C_{60}-serPF fluorescence influx, typically several seconds after C_{60}-serPF injection), (3) after reaching the maximum of C_{60}-serPF fluorescence, typically several minutes after C_{60}-serPF i.v. injection.

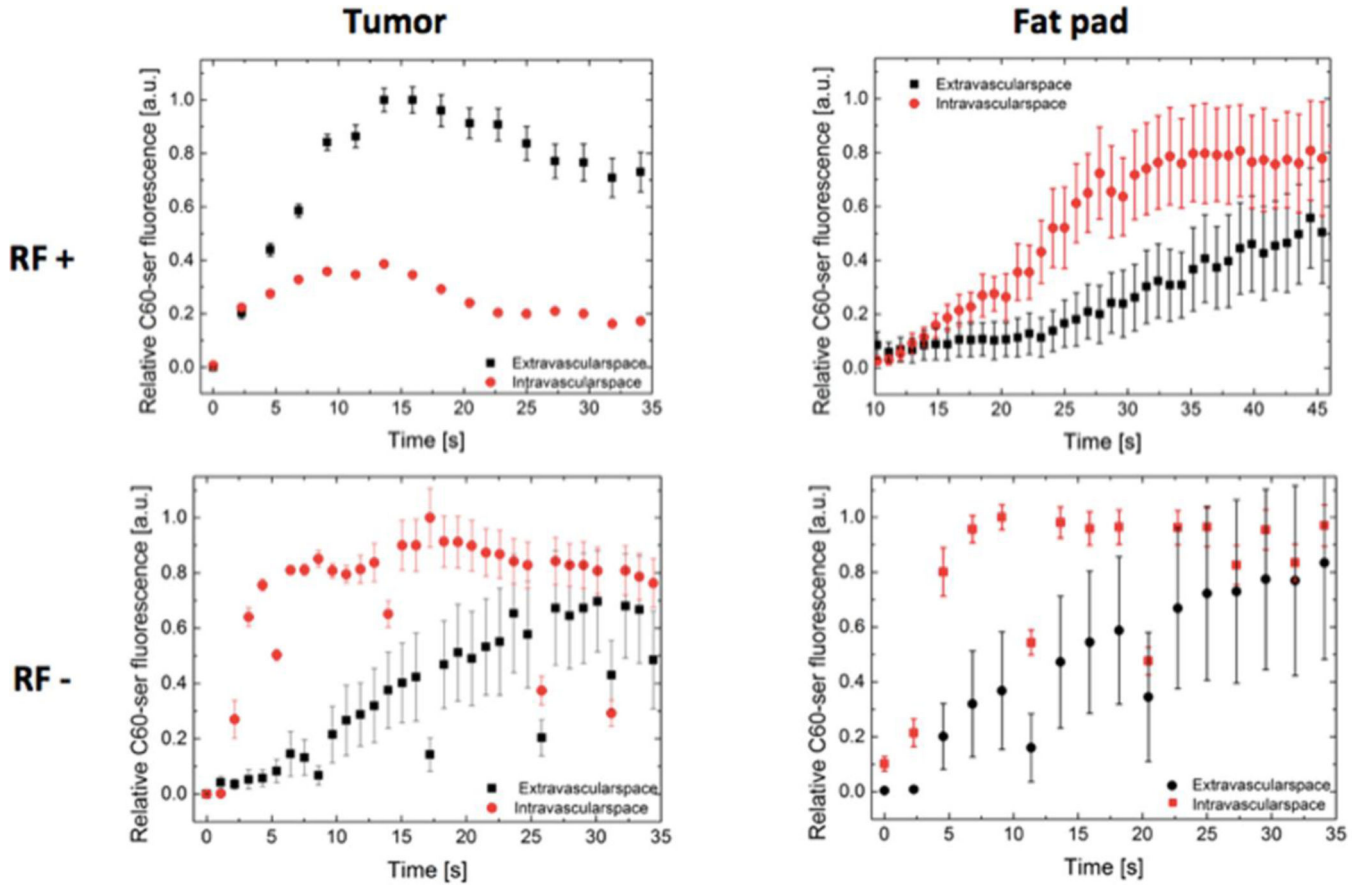

Figure 3.

Representative images of C_{60}-serPF fluorescence kinetics in extravascular and intravascular image compartments. Each point represents the mean of five summed intensities (intensity values summed across compartments for each time point) corresponding to five incrementally applied binary thresholds for C_{60}-serPF fluorescence (663–738 nm) based on least frequent high intensity pixels within the post-injection video image. Error bars denote standard deviation of fluorescence intensity at the selected thresholds. Relative fluorescence refers to the intensity values normalized to maximum intensity of each graph. Time point t=0 marks the video frame of the first appearance of C60-serPF fluorescence in the FOV.

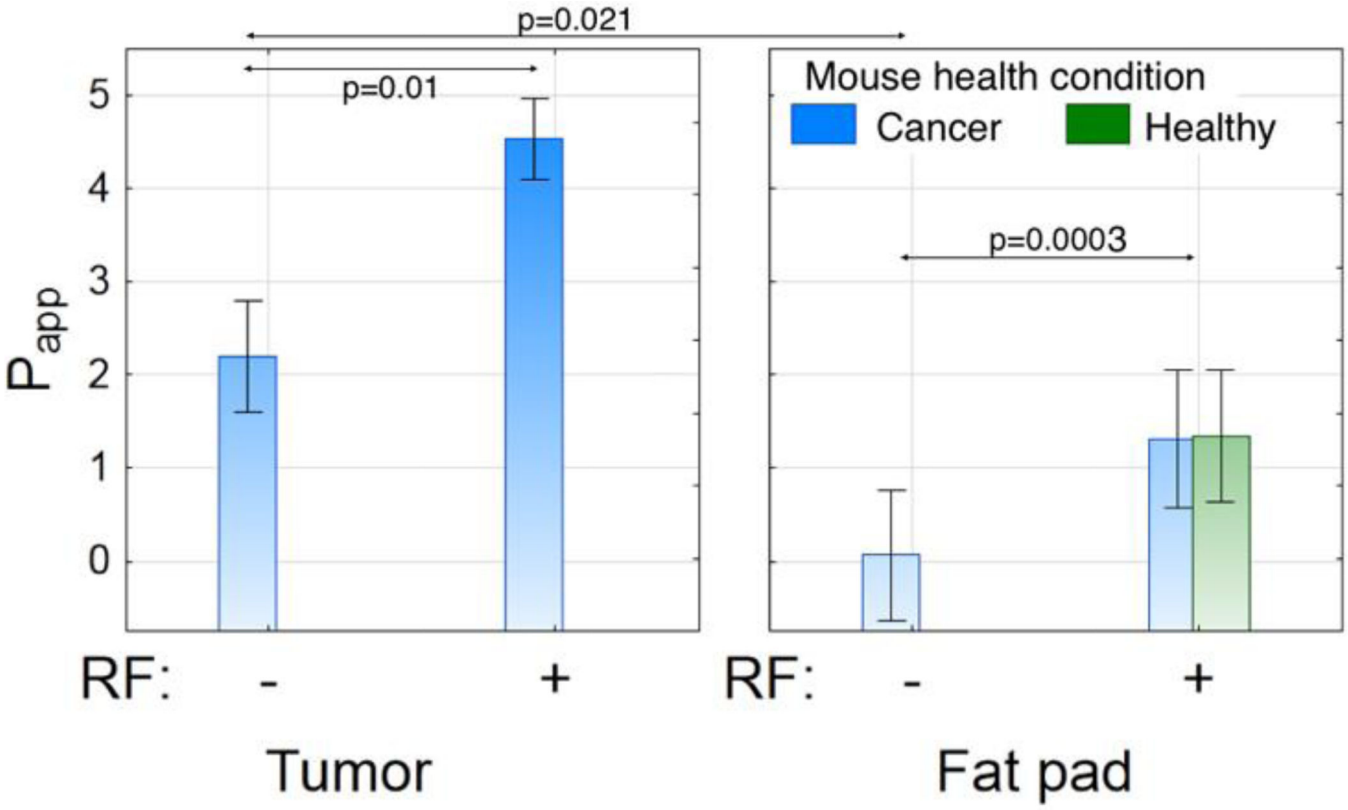

Figure 4.

Apparent permeability (P_{app}) evaluated for tumor (left) and fat pad tissue (right) with and without RF. The effect of RF on normal vasculature in the mammary fat pad was studied in tumor-bearing (red) and tumor-free mice (blue). Data are presented as mean value ± SEM. Statistical significance of the RF effect on P_{app} in tumor tissue is p=0.0153 (U test), while for fad pad, p=0.0003 (U test). The difference between all tumor and fat pad P_{app} values (RF excluded as a factor) was evaluated via ANOVA and is characterized by p<0.0001. Overall RF influence (tissue type excluded as a factor) is also highly significant (p=0.0022).

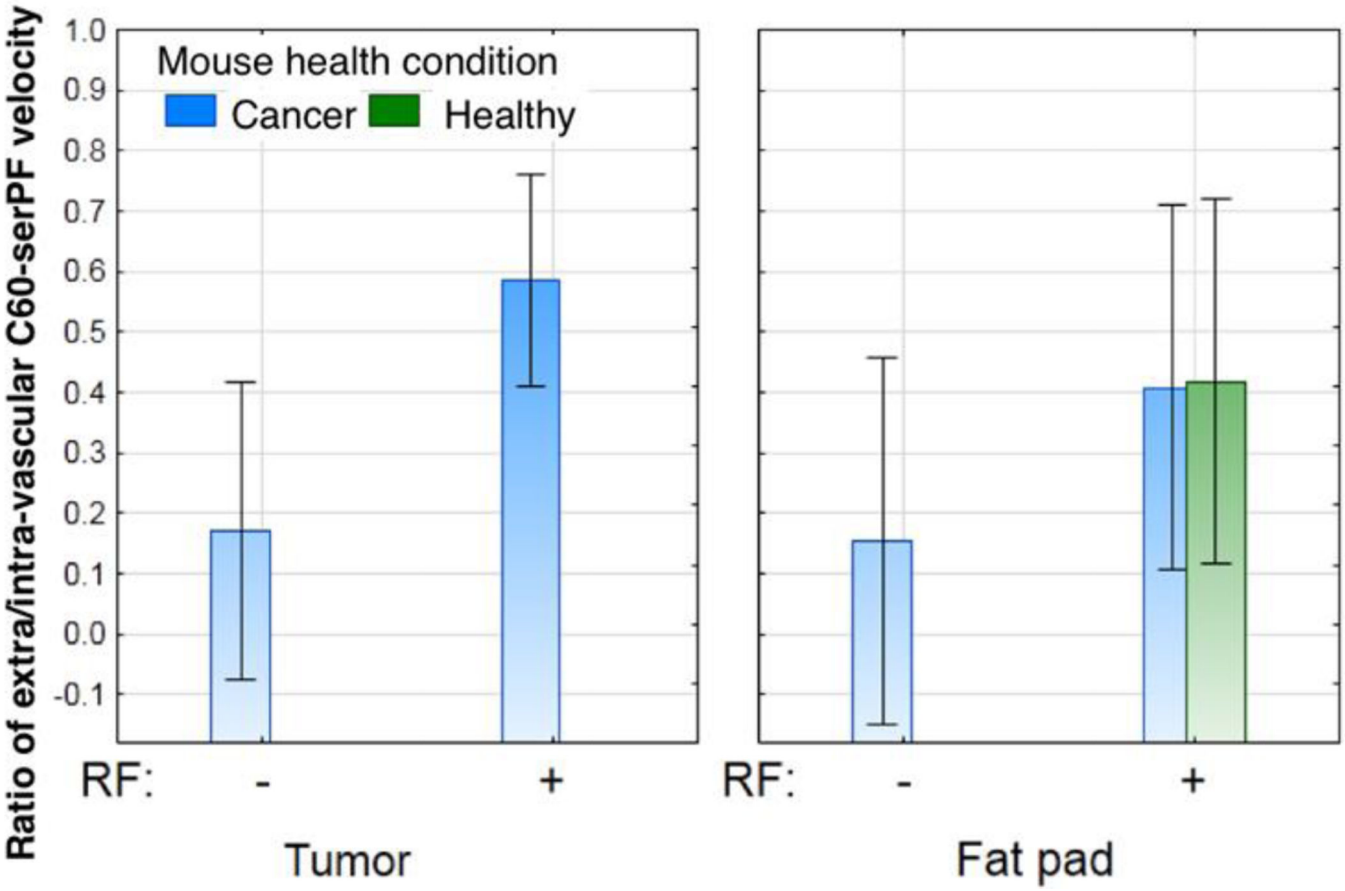

Figure 5.

Ratio of extravascular to intravascular C_{60}-serPF-influx velocity after CM-RFH (+) or control treatment (-) of tumor (left) or fat pad tissue (right) in tumor bearing (red) or cancer free (blue) mice. The velocity of C_{60}-serPF in intravascular and extravascular compartments was calculated as the slope of the linear part of the C_{60}-serPF fluorescence kinetics registered after i.v. bolus C_{60}-serPF injection. To normalize all independent measurements, the C_{60}-serPF fluorescence signal was standardized to maximum fluorescence per influx intensity value (maximum fluorescence per compartment per imaging session =1). ANOVA analysis was used and p=0.2452 was found for CM-RFH treated vs. non-treated tumor tissues.

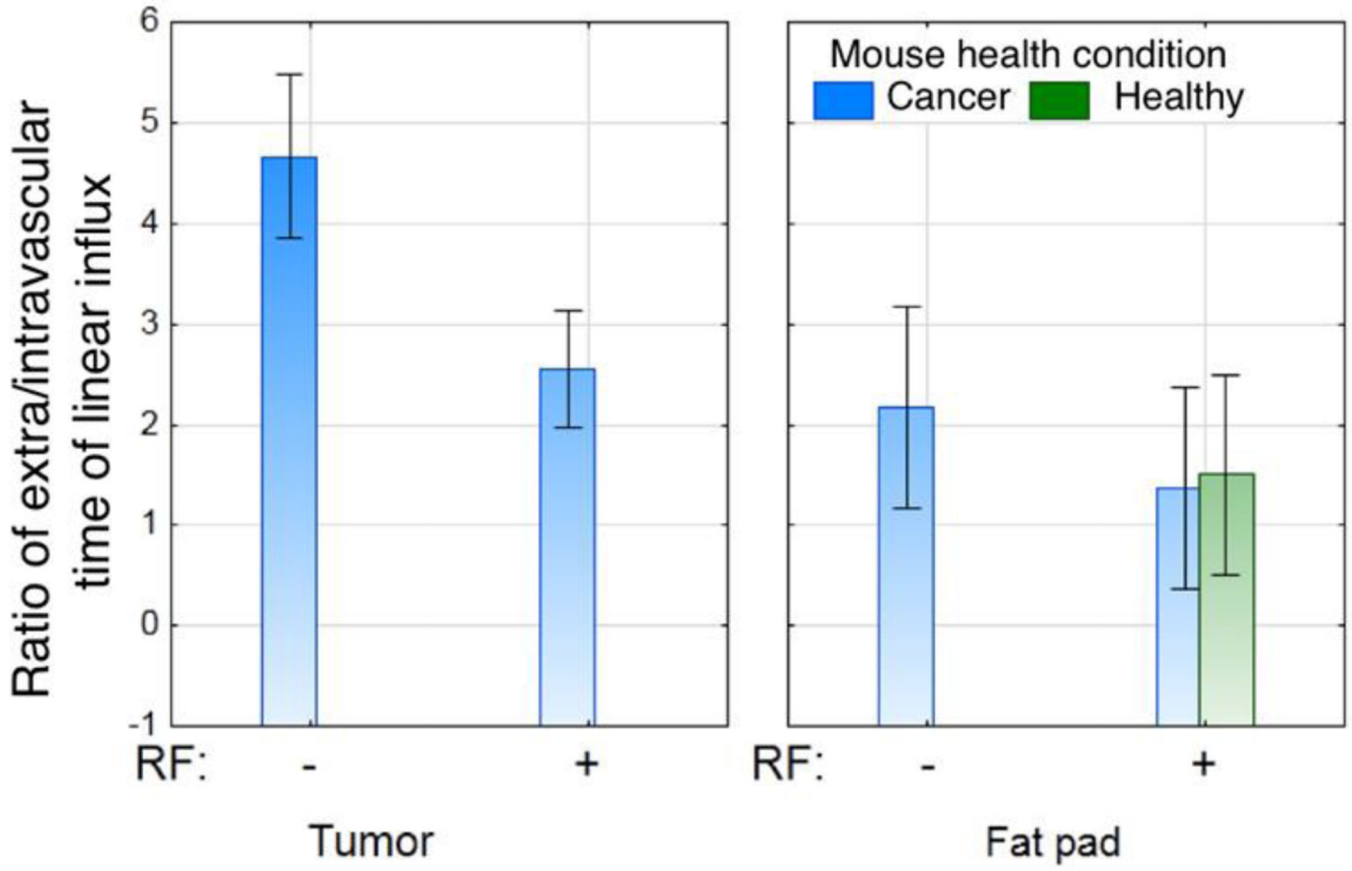

Figure 6.

Ratio of extravascular to intravascular C_{60}-serPF influx time after CM-RFH treatment for tumor and fat pad tissues for stated mouse health condition, with or without cancer. The higher the ratio the longer the time required to reach maximum concentration in the extravascular space, so a lower ratio indicates fast C_{60}-serPF leakage from intravascular to extravascular space. The ANOVA analysis denotes the RF influence in tumor tissue with p=0.1967.